Bacterial glycocalyx integrity drives multicellular swarm biofilm dynamism

Fares Saïdi[1,2,†], Nicolas Y. Jolivet[1,2,†], David J. Lemon[3], Arnaldo Nakamura[1], Anthony G. Garza[3], Frédéric J. Veyrier[1], Salim T. Islam[1,2*]

[1] Institut National de la Recherche Scientifique (INRS) — Centre Armand-Frappier Santé Biotechnologie, Université du Québec, Institut Pasteur International Network, Laval, QC, Canada

[2] PROTEO, the Quebec Network for Research on Protein Function, Engineering, and Applications, Université Laval, Quebec, QC, Canada

[3] Department of Biology, Syracuse University, Syracuse, NY, USA

[†]equal contribution

*corresponding author

Salim T. Islam

E-mail: salim.islam@inrs.ca

Phone: (+1) 450-687-5010 ext. 8897

ABSTRACT

Bacterial surface exopolysaccharide (EPS) layers are key determinants of biofilm establishment and maintenance, leading to the formation of higher-order 3D structures conferring numerous survival benefits to a cell community. In addition to a specific EPS glycocalyx, we recently revealed that the social δ-proteobacterium *Myxococcus xanthus* secretes a novel biosurfactant polysaccharide (BPS), with both EPS and BPS polymers required for type IV pilus (T4P)-dependent swarm expansion via spatio-specific biofilm expression profiles. Thus the synergy between EPS and BPS secretion somehow modulates the multicellular lifecycle of *M. xanthus*. Herein, we demonstrate that BPS secretion functionally-activates the EPS glycocalyx via its destabilization, fundamentally altering the characteristics of the cell surface. This impacts motility behaviours at the single-cell level as well as the aggregative capacity of cells in groups via EPS fibril formation and T4P assembly. These changes modulate structuration of swarm biofilms via cell layering, likely contributing to the formation of internal swarm polysaccharide architecture. Together, these data reveal the manner by which the interplay between two secreted polymers induces single-cell changes that modulate swarm biofilm communities.

INTRODUCTION

The detection of glycocalyces surrounding bacterial cells remains a seminal discovery in bacterial physiology, giving rise to the biofilm concept for surface-attached microbial community growth within a polysaccharide matrix (1). Within a biofilm, bacteria can physically interact, be protected from external stressors (e.g. antibiotics, reactive oxygen species, dehydration, etc.), replicate, communicate via secreted signals, and differentiate their functions (2, 3). While the importance of secreted polysaccharides for biofilm formation is widely appreciated, the mechanisms by which these polymers promote 3D matrix structuration and the cellular organization within are areas of intense study (4).

Robust biofilm existence is exemplified by the social multicellular lifecycle of *Myxococcus xanthus*, a predatory Gram-negative δ-proteobacterium (2, 5, 6). Groups of *M. xanthus* cells are encased within a secreted polysaccharide matrix, promoting intimate contacts. On surfaces, swarms of such cells are able to cooperatively predate prey microorganisms, saprophytically feeding on the degradation products. When nutrients become scarce, *M. xanthus* cells within a swarm biofilm secrete a signalling molecule that accumulates to a certain local threshold above which the developmental program is initiated, leading to the aggregation of thousands of cells and the formation of fruiting bodies. Functional differentiation within the swarm leads to three subpopulations, namely (i) myxospore-forming cells within the fruiting body lumen, (ii) peripheral rods that remain at the base of the fruiting body, and (iii) motile foragers that continue their outward trajectory from the initial aggregate (7).

Two motility systems are required to effectuate these complex physiological outcomes, with each being differentially active depending on the nature of the substratum. On hard surfaces, gliding (i.e. “adventurous” [A]) motility predominates, mediated by substratum

coupling and directed transport of the trans-envelope Agl–Glt machinery at bacterial focal adhesion (bFA) sites (8-10). On soft substrata, cell groups move via type IV pilus (T4P)-dependent (i.e. "social" [S]) motility (11, 12). As a result of these complimentary systems, *M. xanthus* forms highly structured, yet dynamic, biofilms. On hard substrata, *M. xanthus* swarm biofilms expand along a radial vector as well as vertically away from the substratum, resulting in the formation of stratified cell layers (13, 14). Cells within each layer are motile, densely packed, and aligned along their long axes, displaying the properties of an active nematic liquid-crystal state of matter (15). This stratification on hard surfaces may require a functional gliding motility apparatus capable of coupling to an external contacting surface (e.g. the substratum and/or adjacent cells) as layer formation is severely compromised when the substratum-coupling adhesin of the Agl–Glt apparatus (CglB) is absent (10, 13). Prolonged incubation in such biofilms can lead to cells becoming connected via a network of outer-membrane vesicle (OMV) chains and OM tube (OMT) projections (16). In contrast, knowledge of internal swarm architecture on soft substrata is more limited. Of note, the leading edge of such swarms was shown via electron microscopy to contain discreet bundles of aligned cells, encased in Ruthenium Red-stained structures termed polysaccharide "microchannels" (17).

Several long-chain sugar polymers are synthesized by *M. xanthus* in order to modulate its complex lifecycle (18). For cells in development undergoing sporulation, the major spore coat (MASC) polymer is produced to surround myxospores in a protective layer (19, 20). For non-sporulating cells, motility is affected by O-antigen-capped LPS (21-23), as well as a poorly understood "slime" polymer that is proposed to promote adhesion of the Agl–Glt gliding complex to the underlying surface, and which is left behind in trails following transit of gliding cells (24, 25). In addition, the bacterium synthesizes exopolysaccharide (EPS); this is a specific

secreted sugar polymer required for T4P-dependent swarm spreading, which inhibits natural transformation and constitutes the principal matrix polysaccharide in *M. xanthus* biofilms (26-31). Recently, we reported that *M. xanthus* also synthesizes and secretes a novel biosurfactant polysaccharide to the extracellular milieu that is essential for T4P-dependent swarm spreading (32). Within an expanding swarm biofilm, BPS biosynthetic machinery is more highly expressed in the swarm centre, whereas EPS biosynthetic machinery is more highly expressed at the swarm periphery, pointing to spatially-distinct roles for each polysaccharide in the maturation of multicellular swarm biofilms (32).

Each of EPS, BPS, and MASC is synthesized by a separate Wzx/Wzy-dependent pathway, with each respective component given the suffix X (exopolysaccharide), B (biosurfactant), or S (spore coat) (32-35). Individual polysaccharide repeat units in such pathways are assembled on the lipid carrier undecaprenyl pyrophosphate (UndPP) at the cytoplasmic leaflet of the inner membrane (IM), followed by processing via a suite of integral IM proteins (36). Repeat units bound to UndPP are first transported across the IM by the Wzx flippase (37-40). UndPP-linked repeats in the periplasmic leaflet of the IM are then polymerized by Wzy (41-43), to modal lengths specified by Wzz/Wzc polysaccharide co-polymerase (PCP) proteins (41). BPS-pathway WzcB is of the PCP-2A class (44) as it contains an attached cytosolic bacterial tyrosine autokinase (BYK) domain (32, 45, 46). Conversely, EPS- and MASC-pathway WzcX and WzcS (respectively) are of the PCP-2B class as they do not encode a fused BYK domain; instead, these pathways encode standalone WzeX/S BYK proteins (32, 47) for association with their cognate WzcX/S PCP. In turn, Wzb bacterial tyrosine phosphatase (BYP) proteins are also encoded to control the phosphorylation state of PCP-2A Wzc proteins and PCP-2B-associated Wze proteins (48). The *M. xanthus* Wzb BYP (PhpA) has been shown

104 to dephosphorylate BYK WzeS as well as the BYK domain of WzcB (49), implicating Wzb in
105 MASC and BPS biosynthesis. The cytosolic (de)phosphorylation states of PCP-2A Wzc and
106 PCP-2B-associated Wze proteins control not only polymer modal length modulation, but also
107 secretion of the respective heteropolysaccharide across the OM via the Wza translocon (50, 51).
108 A range of activators and inhibitors are known to impact *M. xanthus* EPS biosynthesis
109 (reviewed in (18)), with the Dif chemosensory pathway the most noteworthy (52-54). Positive
110 regulation of EPS production is mediated by (i) the methyl-accepting chemotaxis protein DifA,
111 (ii) the CheW-like coupling protein DifC, (iii) the CheA-like histidine kinase DifE, and (iv) the
112 EpsW response regulator (phosphorylated by DifE) (55-57) Conversely, EPS production is
113 negatively regulated by (i) the DifD response regulator, (ii) the CheC-like phosphatase DifG, and
114 (iii) Nla19, an NtrC-like transcriptional regulator (54, 58). Despite these details, the specific
115 functional links between the Dif pathway and the Wzx/Wzy-dependent EPS biosynthesis system
116 have yet to be identified.
117 While the biosurfactant nature of BPS was previously demonstrated, the mechanism by
118 which it promotes swarm structuration and T4P-dependent spreading was not known (32).
119 Herein, we provide evidence/demonstrate that unlike conventional biosurfactants — which
120 typically function as wetting agents secreted at colony fronts to condition the substratum and
121 promote spreading — a major role of BPS is to change the activation state of the EPS surface
122 glycocalyx. This impacts cell-level and community-scale behaviours leading to altered
123 multicellular outcomes.

RESULTS

BPS-deficient M. xanthus *cells are hyper-aggregative*

Though BPS$^-$ and EPS$^-$ swarms were previously shown to be compromised for T4P-dependent swarm expansion — with the former elaborating a fuzzy morphology and the latter a smooth phenotype — under nutrient limitation BPS$^-$ cells were still able to aggregate and form spore-filled fruiting bodies, similar to WT (but not EPS$^-$) swarms (32) (**Fig. 1**). However, the developmental transition to fruiting bodies for BPS$^-$ swarms could take place at lower initial cell densities compared to WT swarms, suggesting that cells may aggregate more efficiently in BPS$^-$ swarms (32). To specifically probe aggregative differences among *M. xanthus* cell-surface polysaccharide mutants, the real-time ability of cells to auto-aggregate in liquid media was compared, a phenomenon known to be dependent on the presence of cell-surface EPS and an extendable T4P (22, 26, 30, 33, 55, 56, 58-68). While both EPS$^-$ and T4P$^-$ cells remained in suspension, BPS$^-$ cells rapidly auto-aggregated by the first post-mixing time point (10 min), resulting in faster initial unaided sedimentation relative to WT cells; after ~40 min, WT and BPS$^-$ cells in rich media continued to sediment, but at comparable rates, consistent with continued metabolism (**Fig. 2A**). The same rapid auto-aggregation phenotype at the same post-mixing time point (10 min) was observed for BPS$^-$ cells (relative to WT) under non-metabolizing conditions in minimal buffer, with the auto-aggregation levelling off at ~40 min (**Fig. 2B**). Together, these cell-level hyper-aggregation data (i) help explain fruiting body formation for BPS$^-$ swarms at lower cell densities (32), (ii) suggest that T4P may indeed be extendable in BPS$^-$ cells, and (iii) are consistent with differences in the general surface properties of BPS$^-$ cells.

BPS-deficient M. xanthus *cells can extend T4P*

To directly probe T4P assembly, WT, BPS$^-$ and EPS$^-$ cells from liquid culture were analyzed via transmission electron microscopy (TEM). As expected, from the poles of WT cells, numerous T4P projections could be observed, including both thin filaments (likely single pili) and thick filaments (likely bundles of pili); the presence of T4P bundles is supported by the observation that at certain points along the thick filament, branching occurred, with the new offshoots resembling thin filaments (**Fig. 2C**). While no EPS$^-$ cells were observed with attached T4P projections emanating from a cell pole, thin T4P-like filaments were detected on the grid (**Fig. 2C**). This may suggest that EPS$^-$ cells can still assemble a T4P, but that the presence of cell-surface EPS contributes to strengthening the apparatus. Intriguingly, BPS$^-$ cells were observed to extend T4P, but they were not as prevalent as in WT cells; moreover, the T4P filaments detected in BPS$^-$ cells were typically shorter than those in WT cells, and not found in presumed thick T4P bundles (**Fig. 2C**). Thus while BPS$^-$ cells can still extrude T4P projections, the assembly of these apparatus appears to be compromised relative to WT cells, helping to explain the deficiency in T4P-dependent motility in BPS$^-$ cells (**Fig. 1**) (32).

Increased Trypan Blue-retention by BPS⁻ cells is inconsistent with EPS overproduction

Retention of Trypan Blue dye is used as a readout for *M. xanthus* cell-surface EPS levels (30, 58, 69). Intriguingly, despite compromised T4P-dependent swarm spreading (32, 33), BPS-pathway mutants Δ*wzcB*, Δ*wzcB*$_{BYK}$, Δ*wzaB*, and Δ*wzaB* Δ*wzcB* — in which periplasmic BPS polymerization should be permitted but secretion compromised — reproducibly bound more Trypan Blue than WT cells (combined interquartile range of 102–133% of WT) (**Fig. 2D**) (32). This dye-retention difference was manifested despite equivalent levels of the same cell-associated EPS sugars detected in WT and BPS⁻ cells (32). However, the abovementioned four BPS-pathway mutant strains still bound significantly less Trypan Blue than the Δ*difG* strain (interquartile range of 113–202% of WT) (**Fig. 2D**). The latter is a mutant in the Dif chemosensory pathway in which EPS production is no longer negatively-regulated, resulting in increased EPS production; this is compared to a Δ*difE* strain in which EPS production is downregulated (**Fig. 2D**) (55, 56, 58, 70). In fact, EPS overproduction does not significantly compromise T4P-dependent swarm spreading relative to a BPS deficiency (**Fig. 1B**), which severely impairs swarm spreading (32). Taken together with the comparative dye-retention analyses of EPS regulatory mutants (**Fig. 2D**), these data are consistent with the elevated retention of Trypan Blue by the abovementioned BPS-pathway mutants not being due to EPS overproduction. Instead, this may point to differences in surface properties between WT and BPS⁻ cells.

BPS deficiency decreases the relative cell-surface hydrophobicity of M. xanthus

To probe the physical properties of WT and BPS$^-$ cell surfaces, both strains were subjected to MATH (microbial adhesion to hydrocarbons) testing to probe relative differences in cell-surface hydrophobicity (71). Cells of either strain were resuspended in (aqueous) liquid medium and mixed with the hydrocarbon hexadecane, after which the emulsion was allowed to clear (72). The rationale herein is that the greater the cell-surface hydrophobicity of a particular strain, the more cells removed from suspension through hydrophobic contacts with hexadecane, thus decreasing the turbidity of the suspension (71). Compared to OD_{600} readings taken before hexadecane addition-and-mixing, significantly fewer WT cells remained in suspension (i.e. lower OD_{600}) following emulsion separation compared to BPS$^-$ cells (**Fig. 2E**). These findings do not indicate that WT cells are hydrophobic per se, but rather that the WT cell surface is relatively more hydrophobic compared to that of BPS$^-$ cells. Therefore, BPS secretion increases the relative hydrophobicity of the *M. xanthus* cell surface. Moreover, this dataset further supports the designation of BPS as a biosurfactant since biosurfactants have been extensively reported to change the relative cell-surface hydrophobicity of various bacterial cells (73). Finally, the reduced relative cell-surface hydrophobicity of BPS$^-$ cells may help explain the higher-than-WT amounts of hydrophilic Trypan Blue binding observed for the Δ*wzcB*, Δ*wzcB*$_{BYK}$, Δ*wzaB*, and Δ*wzaB* Δ*wzcB* mutants previously described (**Fig. 2D**) (32).

198 ***BPS secretion is required for EPS surface-fibril formation***

199 Given the multiple datasets pointing towards fundamental cell-surface differences
200 between WT and BPS$^-$ cells (**Fig. 2A-E**), surface morphologies for these strains (as well as EPS$^-$
201 cells) were directly visualized via scanning electron microscopy (SEM). Consistent with
202 previous reports, WT cells were shown to be connected via networks of EPS fibrils, while EPS$^-$
203 cells lacked any such connections (16, 55, 63, 74-79) (**Fig. 2F**). Interestingly, while BPS$^-$ cells
204 still produce EPS (32) (**Fig. 2D**), no inter-cell fibril networks were observed for this strain (**Fig.**
205 **2F**). This may indicate that while EPS by itself is tightly held by individual cells, the secretion
206 of BPS serves to sufficiently destabilize or loosen the cell-surface EPS glycocalyx, thus
207 promoting fibril formation and inter-cell connections.

208 ***EPS glycocalyx destabilization impacts single-cell behaviour***

209 Since BPS$^-$ cells are capable of forming fruiting bodies (**Fig. 1A**) (32), this suggests that
210 BPS$^-$ cells can still perform single-cell gliding motility, which is required for efficient fruiting
211 body formation (80). For swarms grown on hard 1.5% agar, flare projections were observed
212 emanating from the edge of the inoculated spot, a tell-tale sign of gliding motility by BPS$^-$ cells
213 (**Fig. 1A**). By way of severe oblique illumination of the samples, we were also able to visualize
214 the furrow network left behind in the agar by lead gliding cells at the swarm edge (**Fig. 1A**).
215 Previously revealed in detail by others using 3D profilometry, these physical depressions in the
216 agar substratum were revealed to be the source of phase-bright trails classically attributed to
217 slime deposition by *M. xanthus* cells gliding on agar (81). All strains tested produced furrows,
218 indicating that the presence or absence of EPS and/or BPS does not qualitatively impact the
219 formation of these substratum depressions. Moreover (while not possible to distinguish between
220 single cells and cell groups), additional cells were detected following the path of the various
221 furrows (**Fig. 1A**), supporting the notion of sematectonic stigmergic coordination for the
222 phenomenon of trail following by *M. xanthus* cells on agar (82). At the single-cell level, the
223 presence of a compacted surface glycocalyx in BPS$^-$ cells, or the complete absence of this layer
224 in EPS$^-$ cells, resulted in faster gliding motility than in WT cells (**Fig. 3A**). Compared to BPS$^-$
225 or EPS$^-$ cells, this may indicate that the bulk volume of the destabilized EPS surface layer in WT
226 cells adversely affects gliding efficiency.

227 We next probed the frequency at which single cells reversed their gliding direction. Cells
228 were imaged at 30 s intervals for 50 frames. To avoid unintentionally lowering reversal
229 frequency averages (by including cells tracked for a short time in which a reversal may not have
230 yet manifested), we only analyzed cells continuously tracked for 30 or more frames. Cells

deficient in EPS secretion were observed to reverse their gliding direction less frequently compared to WT cells (**Fig. 3B**), consistent with previous reports of lower reversal frequencies in Dif-pathway mutants in which EPS production is compromised (68, 83). Conversely, BPS$^-$ cells were found to reverse their gliding direction more frequently than WT cells (**Fig. 3B**). Together, these data point to not only the general importance of EPS in regulating reversal frequency, but also its "activation state" as determined by the effects of BPS.

Given the differences in single-cell gliding behaviours described above, we examined the polymertropism responses of EPS$^-$ and BPS$^-$ cells. Polymertropism is a gliding motility-dependent process. It is measured via changes of the swarm aspect ratio, i.e. comparisons of changes in "east–west" expansion vs "north–south" expansion on an agar plate in response to the insertion of a small length of tubing between the edge of the agar and the "northern" wall of the Petri dish. The net effect of this agar compression is to align the polymers in the substratum matrix, allowing *M. xanthus* and other bacteria to preferentially spread in the "east–west" direction of the aligned substratum polymers (10, 84-86). While no significant differences in polymertropism responses were detected between WT and EPS$^-$ swarms, BPS$^-$ swarms demonstrated a remarkably enhanced capacity to spread in the "east–west" direction on compressed agar (**Fig. 3C**). This is the first known description of a hyper-polymertropic *M. xanthus* strain. While specific cellular factors contributing to the polymertropism response remain poorly understood, our data suggest that the presence of EPS as well as increased gliding speed may contribute to this enhanced "east–west" swarm expansion in response to mechanical changes in the substratum. The secretion of BPS thus affects *M. xanthus* behaviours at multiple levels of biological organization, from entire communities down to single cells.

253 ***BPS secretion is required for cell stratification within swarms***

254 We next sought to probe potential ultrastructural differences in swarm architecture
255 leading to compromised T4P-dependent colony expansion. To highlight internal structures as
256 per a previous report (17), spreading swarms were treated with Ruthenium Red, a polycationic
257 dye that interacts with a range of polyanionic targets (87). This was carried out for swarms of
258 WT, as well as the isogenic EPS^{-}, BPS^{-}, and MASC^{-} mutant strains, followed by negative-stain
259 TEM of transversely-cut sections near the swarm edge (**Fig. 4, *inset***). This resulted in electron-
260 dense labelling of the *M. xanthus* cell surface in the absence of EPS, BPS, or MASC secretion
261 (**Fig. 4**). These analyses also revealed pronounced horizontal electron-dense structures
262 separating stratified layers of WT and MASC^{-} cells, with such structures largely absent in BPS^{-}
263 swarms and nonexistent in EPS^{-} swarms (**Fig. 4**). Vertical striations of this electron-dense
264 material — connecting horizontal electron-dense structures above and below to form a self-
265 contained so-called "microchannel" — were not detected (**Fig. 4**). The rod-shaped cells within
266 the layered WT and MASC^{-} swarms, as well as the more irregularly-packed BPS^{-} swarm, were
267 highly aligned along their long axes in the direction of migration, resulting in the round
268 appearance of cells in the cross sections (**Fig. 4**). Cells in BPS^{-} swarms were also more closely-
269 packed together compared to either WT, MASC^{-}, or EPS^{-} swarms (**Fig. 4**).

270 Higher-magnification views of the horizontal electron-dense ribbons revealed these
271 structures to be of heterogeneous composition; in addition to wispy material which could
272 represent one or more accumulated polysaccharide species, enrichments of individual OMVs as
273 well as OMV chains were also observed at these sites (**Fig. 4**).

274 Taken together, these data suggest that the horizontal electron-dense structures (**Fig. 4**)
275 are not required for nematic alignment of cells in these swarms. Furthermore, the close packing

of cells in BPS$^-$ swarms is consistent with BPS$^-$ cells being more highly aggregative (**Fig. 2A,B**), forming fruiting bodies at lower initial cell densities (32), and displaying more compact surface EPS glycocalyces lacking fibril structures (**Fig. 2F**). Finally, the accumulation of various types of material at these horizontal electron-dense ribbons (**Fig. 4**) raises the possibility that these striations are, in essence, exclusion boundaries between different layers of *M. xanthus* cells within a swarm. Further comment on the nature of these horizontal electron-dense structures can be found in the Discussion below.

DISCUSSION

Originally referred to as "slime fibrils/fibers", sinewy structures connecting the surfaces of clustered *M. xanthus* cells have been known for >40 years (88, 89), with the only known requirement being the presence of the cell-surface EPS glycocalyx (55, 63, 74, 75, 78). Given the phenotypic, biochemical, and biophysical data presented herein, we propose that it is not simply the presence of cell-surface EPS that is required to mediate these inter-cell connections in *M. xanthus*, but rather the activation state of the EPS glycocalyx induced by the effects of secreted BPS.

Unfortunately, confusion exists throughout the scientific literature on the use of the abbreviation "EPS", especially for *M. xanthus* research. Various laboratories (including ours) use "EPS" to specifically denote the principal matrix polysaccharide assembled and secreted via the WzxX-WzyX-WzcX-WzeX-WzaX proteins (32, 33, 65). However, "EPS" has also been used to non-specifically refer to diverse secreted polysaccharides (i.e. "exopolysaccharides"). For many bacteriologists, "EPS" has even more broadly come to signify "extracellular polymeric substances", a term that has come to encompass not only secreted polysaccharides, but also polypeptides and polynucleotides. Given theses various uses, particular attention is required when interpreting and comparing findings across diverse publications.

The data presented herein provide complementary insights into the nature of T4P-dependent group motility in *M. xanthus* swarm biofilms, as they implicate the importance of BPS on several levels. Type IV pili in *M. xanthus* are known to interact with cell-surface EPS, which is how *M. xanthus* cells in rafts are proposed to move together, i.e. a T4P from a given cell is able to interact with the surface EPS layer on an adjacent cell, triggering T4P retraction, close cell–cell association, and group movement (26). Previously, single cells were found to move via

T4P extension and retraction on polystyrene surfaces, but only in the presence of a viscous solution of 1% methylcellulose (90, 91). To what exactly then does a *M. xanthus* T4P bind? Though BPS$^-$ cells can extend a T4P (**Fig. 2C**), these apparatus were typically shorter, thinner, and less prevalent than those in WT cells, and it is not known if pili from BPS$^-$ cells are still able to interact with the "non-activated" EPS on adjacent BPS$^-$ cells. Simplistically, the T4P may need to get stuck within the activated EPS matrix in WT cells, something which might not be possible in BPS$^-$ cells. Alternatively, if unable to bind, this could signify that a specific motif on "activated" EPS needs to be recognized by the T4P, and that this motif is not exposed on the glycocalyx of BPS$^-$ cells. Rather than the "stuck-in-goo" hypothesis, additional evidence supports the latter theory. Specifically, that (i) T4P retraction can be triggered by amine-containing polysaccharides (26), and (ii) single-cell T4P motility is possible in an aqueous microfluidic channel atop glass functionalized with a molecular coating of carboxymethylcellulose (92). The latter principal is analogous to that used for chitosan coatings in microfluidic chambers to test single-cell gliding motility on glass substrata (24, 93).

In addition, BPS secretion alters the fundamental properties of the *M. xanthus* cell surface, impacting numerous processes. Importantly, an imbalance in the EPS:BPS secretion ratio in a given cell can alter surface adhesiveness, directly influencing spatiotemporal cell–cell interaction dynamics, and by extension, swarm biofilm architecture. A greater proportion of EPS:BPS in Δ*wzaB* cells (i.e. WT levels of EPS, no BPS) results in swarms displaying a fuzzy morphology on soft agar (32) (**Fig. 1A**). Similarly, robustly increasing the production of EPS (in Δ*difG* cells) may dilute the effect of BPS, resulting in a similar fuzzy swarm morphology (**Fig. 1A**), albeit with a larger surface area (**Fig. 1B**).

However, BPS$^-$ cell traits such as increased gliding speed and more frequent reversals (relative to WT) are more difficult to interpret. Given that EPS$^-$ cells are not aggregative, the apparent increased "stickiness" of BPS$^-$ cells (and presumed stronger association with the substratum) is not believed to lead to appreciably more efficient substratum-coupling of the Agl–Glt machinery. As the EPS glycocalyx is likely more compacted in BPS$^-$ cells, and completely absent in EPS$^-$ cells, we speculate that the bulk volume occupied by the BPS-activated EPS surface layer in WT cells results in suboptimal surface coupling of the gliding machinery. Conversely, overall increased vs. decreased stickiness of BPS$^-$ vs. EPS$^-$ cells (respectively) may indicate a role for mechanical feedback from physical interactions with the substratum influencing properties of the Agl–Glt apparatus at bFA sites and/or the Frz chemosensory system that governs polarity reversals within the cell (94), potentially affecting reversal frequency. The combined effects of increased gliding speed and potential differences in bFA stability and/or Frz system activity may also help explain the hyper-polymertropism observed for BPS$^-$ cells.

The detection of internal Ruthenium Red-labelled structures near the swarm edge presented herein provides important independent support for the overall concept of leading-edge "microchannels" reported by Berleman and colleagues (17). Differences in the numbers of cells contained within layer/channel structures could be attributable to minor variations in initial swarm inoculation (volume, cell density, etc.). However, we remain skeptical of the notion that the Ruthenium Red-labelled structures are mainly composed of EPS. Ruthenium Red is a polycationic dye with a well-documented propensity for binding to a range of anionic targets (87). Originally used as a highly-effective labelling agent for pectin (a galacturonic acid-rich polysaccharide), the dye has since been shown to also bind other anionic polysaccharides, phospholipids, DNA, and proteins (87, 95-98). Though a chemical structure has yet to be

351 determined, the composition of *M. xanthus* EPS has been studied across four publications. In
352 total, arabinose, galactose, *N*-acetyl-galactosamine, glucose, glucosamine, *N*-acetyl-glucosamine,
353 mannose, *N*-acetyl-mannosamine, rhamnose, and xylose sugars have been reported (32, 77, 99,
354 100). However, none of these reported EPS sugars carry a net-negative charge that would favour
355 Ruthenium Red binding; this has lead us to question whether the distinct horizontal ribbons we
356 detected within WT and MASC^{-} swarms (**Fig. 4**), as well as the walls of self-enclosed so-called
357 "microchannel" structures at the WT swarm edge (17), are indeed composed of *M. xanthus* EPS.
358 Of note, extracellular DNA (eDNA) has been previously detected in *M. xanthus* biofilms
359 and shown to bind secreted polysaccharides as well as strengthen the extracellular matrix (101).
360 Moreover, we have herein detected the accumulation of OMVs and OMV chains at the
361 Ruthenium Red-stained layers, material which by definition contains phospholipids as well as
362 phosphate groups linked to the Lipid A motif of its LPS (102) (**Fig. 4**). In addition to
363 polysaccharide, the *M. xanthus* extracellular matrix is also abundant in protein species of largely
364 unknown functions (77, 103). Most intriguingly, BPS may be a strong candidate for the
365 principal Ruthenium Red-labelled substance detected in the mid-swarm horizontal ribbons
366 reported herein (**Fig. 4**) as well as the leading-edge enclosed channel structures previously
367 reported (17). Consider that the BPS polymer is an acidic heteropolysaccharide built of
368 repeating tetrasaccharide units; each tetrasaccharide repeat contains a proximal *N*-acetyl-D-
369 mannosamine, followed by three distal anionic *N*-acetyl-D-mannuronic acid sugars, with the first
370 three sugars of each repeat being randomly acetylated (32). Furthermore, pronounced
371 Ruthenium Red-labelled horizontal striations were not detected in BPS^{-} swarms (**Fig. 4**). In
372 addition, compositional analysis of cell-associated sugars as well as surface-active testing of
373 culture supernatants suggest that BPS is not bound to the cell surface and is instead secreted into

the extracellular milieu (32). The combined effect of a sheet of EPS glycocalyces from adjacent cells could thus be to electrostatically and/or sterically exclude secreted anionic BPS and concentrate it at EPS-free zones between cell layers. It may then be in these levels of a swarm where BPS may fully activate (destabilize) the EPS of adjoining cells, allowing for efficient T4P-mediated swarm expansion. This could also explain why no Ruthenium Red-stained structures could be detected in EPS$^-$ swarms (**Fig. 4**) (17), i.e. the absence of EPS resulted in no exclusion boundaries at which BPS could accumulate. In this manner, the lumen of swarm-edge microchannels would still contain EPS material, but the surrounding Ruthenium Red-binding wall structures would contain BPS. Ultimately, BPS-dependent stratification in swarm biofilms appears to play an important role in community organization and expansion.

Our data may also shed light on findings regarding the proposed effect of the Wzb (PhpA) tyrosine phosphatase on *M. xanthus* EPS production (49). Mori and colleagues reported that a mutant lacking this Wzb tyrosine phosphatase possessed higher levels of phosphorylated (i) BYK protein WzeS (BtkA) and (ii) the BYK domain-containing WzcB (BtkB) (49). These proteins are now known to be a part of the MASC and BPS assembly pathways, respectively (32, 33, 47). Wzb-deficient cells also exhibited faster auto-aggregation in cuvettes compared to WT cells, and were able to aggregate earlier in development resulting in faster fruiting body formation (49). Finally, the amount of Trypan Blue dye bound by Wzb-deficient cells was 134% that of WT cells (49). Accounting for these and other data, the authors concluded that PhpA may have a negative regulatory effect on EPS biosynthesis (49). However, based on (i) the demonstrated dephosphorylation of BPS-pathway WzcB by this Wzb tyrosine phosphatase (49), (ii) the faster auto-aggregation of BPS$^-$ cells (**Fig. 2A,B**), (iii) the more efficient formation of fruiting bodies by BPS$^-$ swarms (32), and (iv) the marginally higher amount of Trypan Blue

bound by BPS^{-} cells relative to WT (**Fig. 2D**) (32), the findings for Wzb-deficient vegetative cells are more in line with a deficiency in BPS production rather than an increase in EPS production. With respect to direct effects of Wzb on the EPS biosynthesis pathway, it remains to be seen whether the Wzb tyrosine phosphatase (which already acts on WzcB and WzeS) also acts on the recently-identified WzeX BYK shown to be essential for EPS biosynthesis (32). To date, the manner by which the Dif chemosensory pathway regulates EPS production is unknown (18). Nonetheless, regulation of the putative phosphorylation state of WzeX is an attractive target for understanding changes in EPS levels during the *M. xanthus* lifecycle.

MATERIALS AND METHODS

Bacterial Cell Culture

The *M. xanthus* strains used in this study are listed in **Table 1**. They were grown and maintained at 32 °C on Casitone-yeast extract (CYE) agar plates or in CYE liquid medium at 32 °C on a rotary shaker at 220 rpm. The *Escherichia coli* strains used for plasmid construction were grown and maintained at 37 °C on LB agar plates or in LB liquid medium. Plates contained 1.5% agar (BD Difco).

Phenotypic Analysis

Exponentially-growing cells were harvested and resuspended in TPM buffer (10 mM Tris-HCl, pH 7.6, 8 mM $MgSO_4$ and 1 mM KH_2PO_4) at the final concentration of OD_{600} 5.0 for gliding, T4P-dependent expansion, and developmental assays. This cell suspension (5 μL) was spotted onto CYE 1.5% agar, CYE 0.5% agar, or CF 1.5% agar for gliding flare, T4P-dependent swarm expansion, or developmental (i.e. fruiting body formation) analysis, respectively. Plates were incubated at 32 °C for 30 h for gliding flares, 72 h for T4P-dependent swarm expansion, and 75 h for fruiting body formation, then photographed with an Olympus SZX16 stereoscope with UC90 4K camera. Gliding flares were imaged using the 2× objective at 8× zoom, using linear colour, with illumination control wheel set halfway between the brightfield cartridge and the open slot on the illumination wheel. For T4P-dependent motility, swarms were imaged using the 0.5× objective at 1× zoom, using linear colour and darkfield illumination. For fruiting bodies, structures were imaged using the 0.5× objective at 2× zoom, using high-quality colour and oblique illumination.

428 ***Transmission Electron Microscopy***

429 For T4P visualization, a 50 µL drop of overnight liquid culture was transferred to a
430 copper grid and incubated at ambient temperature for 5 min. Grids were then dried with
431 bibulous paper, stained with 3% PTA (pH 6.0) (Mecalab) for 2 s, and dried again with bibulous
432 paper. For swarm biofilm cross-sections, swarm samples were fixed in 2.5% glutaraldehyde in
433 cacodylate buffer at pH 7.4 with 0.2M sucrose overnight and then washed three times with
434 cacodylate buffer. Then post-fixed in 1.33% osmium tetroxide in Collidine buffer (pH 7.4) for 1
435 h and stained with 5 mM Ruthenium Red for 1 h at ambient temperature. After dehydration by
436 successive passages through 25, 50, 75, 95% and 100% (twice) solutions of ethanol in water (for
437 30 min each), samples were immersed for 16–18 h in Spurr:acetone (1:1 v/v). Samples were then
438 embedded in Spurr resin (TedPella) before incubation at 60–65 °C for 20–30 h. After
439 polymerization, samples were sectioned (90 – 150 nm) using an ultramicrotome (LKB Brooma -
440 2128 Ultratome). Sections were collected on formvar / carbon-coated copper 200-mesh grids.
441 Samples were stained with 5% uranyl acetate in 50% ethanol for 15 minutes followed by lead
442 citrate for 5 minutes. Imaging for T4P and swarm biofilm cross-sections was carried out using a
443 Hitachi H-7100 transmission electron microscope with AMT XR-111 camera.
444
445 ***Scanning Electron Microscopy***

446 Glass coverslip discs were first washed in 100% EtOH for 1h and left to dry at RT under
447 sterile conditions. The cleaned discs were immersed for 1h at RT in 0.01% poly-L-lysine
448 solution and allowed to dry. Discs were placed one per well in a 24-well polystyrene cell-
449 repellent plate and overlaid with 2 mL of overnight CYE bacterial cultures. Plates were then
450 covered, sealed with Parafilm, and incubated overnight with shaking at 32 ºC. After incubation,

451 the media was removed and the cells attached to the coverslips were fixed in 1 mL of 2.5%
452 glutaraldehyde in 0.1 M cacodylate buffer (pH 7.4) for at least 1 h and washed three times in 1
453 mL of 0.2 M cacodylate buffer for 5 min. After post-fixation in 500 µL of 1.33% osmium
454 tetroxide (in 0.2 M cacodylate buffer) for 1 h, bacteria were dehydrated with increasing ethanol
455 concentrations (25, 50, 75, 95 and 100%). From the 100% EtOH bath, coverslips were critical-
456 point-dried using CO_2 (Leica EM ACE600), coated with 3 nm gold/palladium (Leica CPD300)
457 and examined with a JEOL JSM-7400F scanning electron microscope (3 kV-LEI detector).
458
459 ***Single-Cell Gliding Motility Analysis***
460 For phase-contrast microscopy on agar pads, cells from exponentially-growing cultures
461 were sedimented and resuspended in TPM buffer (OD_{600} 0.7), spotted (3 µL) on a glass
462 coverslip, and overlaid with a 1.5% agar pad prepared with TPM buffer. For motility analysis,
463 cells were left to adhere for 5 min prior to imaging at 32 ºC. Images were obtained using an
464 Axio Observer 7 microscope, with a Plan Apochromat 40× 1.3 oil objective VIS-IR M27 (for
465 total magnification 400×), an Axiocam 512 as camera, and a TL LED as light source (Zeiss).
466 Images were taken at 30 s intervals. The microscope was operated using the Zen 2.6 Pro software
467 suite (Zeiss).
468 Prior to analysis, image stacks were treated in FIJI as follows to optimize tracking: *Step*
469 *1:* Enhance Contrast (0.3%), Normalize, Process All Slices. *Step 2:* Subtract Background
470 (Rolling ball radius of 15.0 pixels, Light background, Process all slices). *Step 3:* Image
471 alignment in stack via StackReg (Translation) plug-in. Cell gliding speeds were then calculated
472 using the MicrobeJ module for FIJI (104): *Step 1:* Under the Bacteria tab, Tracking Parameters
473 were adjusted (Max Entropy, Medial Axis, Area: 18-800, Length: 10-max, Width: 1.5-max),

474 with only cells tracked for a minimum lifespan of 20 frames used for analysis. *Step 2:*
475 Automatically-detected objects were manually curated to remove instances of object merging,
476 background artifact detection, and reference cell switching, followed by comparison of Velocity
477 Means (pixels/frame). *Step 3:* Gliding speeds were converted to "μm/min". Reversals of gliding
478 direction for these tracked cells were manually counted, with a minimum displacement of ~75%
479 of cell length considered a reversal.
480
481 ***Polymertropism Testing***
482 Aspect ratio (AR) vs. time analyses were modified from a published report (84) and were
483 performed as previously described (85). Cells of *M. xanthus* (grown in CYE at 28 °C to ~ 5 ×
484 10^8 cells/mL) were sedimented (4000 × *g*, 10 min), then resuspended in CYE broth to 5 × 10^9
485 cells/mL, and used to inoculate (4 μL) compressed and uncompressed round 85 mm CTTYE
486 agar plates. An ~ 1 cm length of 5.56 mm outer-diameter Tygon tubing was inserted against the
487 plate wall to compress the agar (84), with cells on these plates inoculated 43 mm from the
488 inserted tubing. Following incubation at 30 ºC for 24, 52, 90, 120, and 144 h, colony perimeters
489 were marked at each interval. The AR of each swarm was then calculated for each time point by
490 taking the quotient of the colony width and colony height; a round swarm will produce an AR
491 near-or-equal to one, whereas an elongated swarm will produce an AR > 1. For each replicate
492 dataset, linear best-fit lines were plotted, followed by determination of the slope (i.e. AR/time).
493 Average slope values were calculated for each strain and normalized as a percentage of the
494 AR/time for the WT strain.
495
496

497 ***Auto-Aggregation Testing***

498 Using a modified version of an auto-aggregation protocol (60), overnight *M. xanthus*
499 cultures (10 mL) were sedimented in 15 mL conical tubes (4000 × *g*, 5 min), followed by
500 resuspension of pellets in TPM buffer (10 mL) and OD_{600} determination using disposable
501 cuvettes. Specific resuspension volumes were aspirated and sedimented in a microfuge tube
502 (4000 × *g*, 5 min); pellets were resuspended in 1 mL CYE broth or TPM buffer to a final OD_{600}
503 of 0.5, followed by transfer to a polystyrene spectrophotometer cuvette. Samples were
504 vigorously aspirated/ejected in the cuvette for 10 s using a p200 micropipette, followed by
505 immediate reading of the OD_{600} (t = 0). Subsequent OD_{600} readings were obtained at 10 min
506 intervals up to 150 min of monitoring. Finally, all OD_{600} readings were normalized to the OD_{600}
507 determined at t = 0 for each sample.
508
509 ***Cell-Surface Hydrophobicity Testing***

510 To analyze relative differences in cell-surface hydrophobicity, we employed a modified
511 version of the classic microbial adhesion to hydrocarbons (MATH) assay (71, 72). Based on the
512 OD_{600} of *M. xanthus* overnight cultures (12.5 mL CYE) measured via NanoDrop 2000c
513 spectrophotometer (Thermo), sufficient culture volume was removed, sedimented (6000 × *g*, 5
514 min) in 2 mL conical tubes, followed by pellet resuspension in 4 mL fresh CYE medium via
515 using a p1000 micropipette to a final OD_{600} of 1.0. The OD_{600} of the equilibrated 4 mL
516 resuspensions (i.e. Mix 1) was read in a quartz cuvette. Cell suspensions were then transferred to
517 a new 15 mL conical tube using a p1000 micropipette, mixed via vortex (maximum speed, 20 s),
518 then transferred back to the quartz cuvette for OD_{600} determination (i.e. Mix 2); this step was
519 performed as an internal control to ensure that downstream changes in OD_{600} were not simply

due to further mixing of the sample, particularly for hyper-aggregative strains. Samples were returned via aspiration with a p1000 micropipette to the same 15 mL conical tube, followed by addition of 300 µL hexadecane (Sigma). To generate emulsions, cell–hydrocarbon mixtures were blended via vortex (maximum speed, 20 s), then rapidly transferred back to the quartz cuvette using a p1000 micropipette (i.e. Mix 3). The OD_{600} of this resuspension was immediately determined (t = 0), followed by readings at 5 min intervals for the next three data points. After the initial 15 min of monitoring, emulsion separation was further monitored at 10 min intervals to a final monitoring time of 65 min. All OD_{600} readings were normalized to the initial OD_{600} determined for samples at the "Mix 1" stage of processing.

Trypan Blue Dye Retention

Trypan Blue dye-retention analysis was performed as previously described (32). In brief, cells grown overnight in CYE cultures were resuspended to OD_{600} 1.0 in TPM. Resuspended cells or a cell-free blank (900 µL) were added together with Trypan Blue stock solution (100 µL) to a microfuge tube, then briefly pulsed (1 s) on a vortex mixer. Samples were incubated at room temperature, in an aluminum foil-covered tube rack, on a rocker platform (1 h) to permit dye binding by the cells. Samples were then sedimented (16 000 × g, 5 min), followed by transfer of the top 900 µL of blank or clarified supernatant to a disposable spectrophotometer cuvette. Using the cell-free "TPM + Trypan Blue" sample, the spectrophotometer was blanked (585 nm). For each clarified supernatant, the absorbance at the same wavelength (A_{585}) was determined. Absorbance values were then normalized to A_{585} for the WT sample.

ACKNOWLEDGEMENTS

The authors would like to thank (i) Éric Déziel for insightful discussions and troubleshooting regarding hydrophobicity testing and (ii) Philippe Constant for valuable input on biostatistics. A Discovery operating grant (RGPIN-2016-06637) from the Natural Sciences and Engineering Research Council of Canada and a Discovery Award (2018-1400) from the Banting Research Foundation fund work in the lab of S.T.I. as well as studentships for F.S. and N.Y.J.; both are also recipients of graduate studentships from the PROTEO research network. The funders had no role in study design, data collection and interpretation, or the decision to submit the work for publication.

REFERENCES

1. **Costerton JW, Geesey G, Cheng KJ.** 1978. How bacteria stick. Sci. Am. **238:**86-95.

2. **O'Toole G, Kaplan HB, Kolter R.** 2000. Biofilm formation as microbial development. Annu. Rev. Microbiol. **54:**49-79.

3. **Zhang Y, Ducret A, Shaevitz J, Mignot T.** 2012. From individual cell motility to collective behaviors: insights from a prokaryote, *Myxococcus xanthus*. FEMS Microbiol. Rev. **36:**149-164.

4. **Limoli DH, Jones CJ, Wozniak DJ.** 2015. Bacterial extracellular polysaccharides in biofilm formation and function. Microbiol. Spectr. **3**.

5. **Monds RD, O'Toole GA.** 2009. The developmental model of microbial biofilms: ten years of a paradigm up for review. Trends Microbiol. **17:**73-87.

6. **Van Gestel J, Vlamakis H, Kolter R.** 2015. Division of labor in biofilms: the ecology of cell differentiation, p. 67-97, Microbial Biofilms.

7. **Konovalova A, Petters T, Søgaard-Andersen L.** 2010. Extracellular biology of *Myxococcus xanthus*. FEMS Microbiol. Rev. **34:**89-106.

8. **Islam ST, Mignot T.** 2015. The mysterious nature of bacterial surface (gliding) motility: a focal adhesion-based mechanism in *Myxococcus xanthus*. Semin. Cell Dev. Biol. **46:**143-154.

9. **Faure LM, Fiche J-B, Espinosa L, Ducret A, Anantharaman V, Luciano J, Lhospice S, Islam ST, Tréguier J, Sotes M, Kuru E, Van Nieuwenhze MS, Brun Y, Théodoly O, L A, Nollmann M, Mignot T.** 2016. The mechanism of force transmission at bacterial focal adhesion complexes. Nature **539:**530-535.

10. **Islam ST, My L, Jolivet NY, Belgrave AM, Fleuchot B, Brasseur G, Faure LM, Sharma G, Lemon DJ, Saïdi F, Fiche J-B, Bratton BP, Singer M, Garza AG, Nollmann M, Shaevitz JW, Mignot T.** 2020. CglB adhesins secreted at bacterial focal adhesions mediate gliding motility. bioRxiv**:**2020.2007.2022.216333.

11. **Wu SS, Kaiser D.** 1995. Genetic and functional evidence that Type IV pili are required for social gliding motility in *Myxococcus xanthus*. Mol. Microbiol. **18:**547-558.

12. **Chang Y-W, Rettberg LA, Treuner-Lange A, Iwasa J, Søgaard-Andersen L, Jensen GJ.** 2016. Architecture of the type IVa pilus machine. Science **351:**aad2001-2001-aad2001-2007.

13. **Kaiser D, Warrick H.** 2014. Transmission of a signal that synchronizes cell movements in swarms of *Myxococcus xanthus*. Proc. Natl. Acad. Sci. USA.

14. **Curtis PD, Taylor RG, Welch RD, Shimkets LJ.** 2007. Spatial organization of *Myxococcus xanthus* during fruiting body formation. J. Bacteriol. **189:**9126-9130.

15. **Copenhagen K, Alert R, Wingreen NS, Shaevitz JW.** 2020. Topological defects induce layer formation in *Myxococcus xanthus* colonies. arXiv.

16. **Remis JP, Wei D, Gorur A, Zemla M, Haraga J, Allen S, Witkowska HE, Costerton JW, Berleman JE, Auer M.** 2013. Bacterial social networks: structure and composition of *Myxococcus xanthus* outer membrane vesicle chains. Environ. Microbiol. **16:**598-610.

17. **Berleman JE, Zemla M, Remis JP, Liu H, Davis AE, Worth AN, West Z, Zhang A, Park H, Bosneaga E, van Leer B, Tsai W, Zusman DR, Auer M.** 2016. Exopolysaccharide microchannels direct bacterial motility and organize multicellular behavior. ISME J.

18. **Pérez-Burgos M, Søgaard-Andersen L.** 2020. Biosynthesis and function of cell-surface polysaccharides in the social bacterium *Myxococcus xanthus*. Biol. Chem. **(advance online):**n/a.

19. **Kottel RH, Bacon K, Clutter D, White D.** 1975. Coats from *Myxococcus xanthus*: characterization and synthesis during myxospore differentiation. J. Bacteriol. **124:**550-557.

20. **Wartel M, Ducret A, Thutupalli S, Czerwinski F, Le Gall A-V, Mauriello EMF, Bergam P, Brun YV, Shaevitz J, Mignot T.** 2013. A versatile class of cell surface directional motors gives rise to gliding motility and sporulation in *Myxococcus xanthus*. PLoS Biol. **11:**e1001728.

21. **Fink JM, Zissler JF.** 1989. Defects in motility and development of *Myxococcus xanthus* lipopolysaccharide mutants. J. Bacteriol. **171:**2042-2048.

22. **Bowden MG, Kaplan HB.** 1998. The *Myxococcus xanthus* lipopolysaccharide O-antigen is required for social motility and multicellular development. Mol. Microbiol. **30:**275-284.

23. **Pérez-Burgos M, García-Romero I, Jung J, Valvano MA, Søgaard-Andersen L.** 2019. Identification of the lipopolysaccharide O-antigen biosynthesis priming enzyme and the O-antigen ligase in *Myxococcus xanthus*: critical role of LPS O-antigen in motility and development. Mol. Microbiol. **112:**1178-1198.

24. **Ducret A, Valignat M-P, Mouhamar F, Mignot T, Theodoly O.** 2012. Wet-surface-enhanced ellipsometric contrast microscopy identifies slime as a major adhesion factor during bacterial surface motility. Proc. Natl. Acad. Sci. USA **109:**10036-10041.

25. **Ducret A, Fleuchot B, Bergam P, Mignot T.** 2013. Direct live imaging of cell–cell protein transfer by transient outer membrane fusion in *Myxococcus xanthus*. eLife **2:**e00868.

26. **Li Y, Sun H, Ma X, Lu A, Lux R, Zusman D, Shi W.** 2003. Extracellular polysaccharides mediate pilus retraction during social motility of *Myxococcus xanthus*. Proc. Natl. Acad. Sci. USA. **100:**5443-5448.

27. **Palsdottir H, Remis JP, Schaudinn C, O'Toole E, Lux R, Shi W, McDonald KL, Costerton JW, Auer M.** 2009. Three-dimensional macromolecular organization of cryofixed *Myxococcus xanthus* biofilms as revealed by electron microscopic tomography. J. Bacteriol. **191:**2077-2082.

28. **Smaldone GT, Jin Y, Whitfield DL, Mu AY, Wong EC, Wuertz S, Singer M.** 2014. Growth of *Myxococcus xanthus* in continuous-flow-cell bioreactors as a method for studying development. Appl. Environ. Microbiol. **80:**2461-2467.

29. **Hu W, Lux R, Shi W.** 2013. Analysis of exopolysaccharides in *Myxococcus xanthus* using confocal laser scanning microscopy, p. 121-131. *In* Delcour AH (ed.), Bacterial Cell Surfaces: Methods and Protocols. Humana Press, Totowa, NJ.

30. **Hu W, Wang J, McHardy I, Lux R, Yang Z, Li Y, Shi W.** 2012. Effects of exopolysaccharide production on liquid vegetative growth, stress survival, and stationary phase recovery in *Myxococcus xanthus*. J. Microbiol. **50:**241-248.

31. **Wang J, Hu W, Lux R, He X, Li Y, Shi W.** 2011. Natural transformation of *Myxococcus xanthus*. J. Bacteriol. **193:**2122-2132.

32. **Islam ST, Vergara Alvarez I, Saïdi F, Guiseppi A, Vinogradov E, Sharma G, Espinosa L, Morrone C, Brasseur G, Guillemot J-F, Benarouche A, Bridot J-L, Ravicoularamin G, Cagna A, Gauthier C, Singer M, Fierobe H-P, Mignot T, Mauriello EMF.** 2020. Modulation of bacterial multicellularity via spatio-specific polysaccharide secretion. PLOS Biol. **18:**e3000728.

33. **Pérez-Burgos M, García-Romero I, Jung J, Schander E, Valvano MA, Søgaard-Andersen L.** 2020. Characterization of the exopolysaccharide biosynthesis pathway in *Myxococcus xanthus*. J. Bacteriol.**:**JB.00335-00320.

34. **Pérez-Burgos M, García-Romero I, Valvano MA, Søgaard-Andersen L.** 2020. Identification of the Wzx flippase, Wzy polymerase and sugar-modifying enzymes for spore coat polysaccharide biosynthesis in *Myxococcus xanthus*. Mol. Microbiol. **113:**1189-1208.

35. **Islam ST, Lam JS.** 2014. Synthesis of bacterial polysaccharides via the Wzx/Wzy-dependent pathway. Can. J. Microbiol. **60:**697-716.

36. **Islam ST, Taylor VL, Qi M, Lam JS.** 2010. Membrane topology mapping of the O-antigen flippase (Wzx), polymerase (Wzy), and ligase (WaaL) from *Pseudomonas aeruginosa* PAO1 reveals novel domain architectures. mBio **1:**e00189-00110.

37. **Liu D, Cole RA, Reeves PR.** 1996. An O-antigen processing function for Wzx (RfbX): a promising candidate for O-unit flippase. J. Bacteriol. **178:**2102-2107.

654 38. **Islam ST, Fieldhouse RJ, Anderson EM, Taylor VL, Keates RAB, Ford RC, Lam JS.**
655 2012. A cationic lumen in the Wzx flippase mediates anionic O-antigen subunit
656 translocation in *Pseudomonas aeruginosa* PAO1. Mol. Microbiol. **84:**1165-1176.

657 39. **Islam ST, Eckford PDW, Jones ML, Nugent T, Bear CE, Vogel C, Lam JS.** 2013.
658 Proton-dependent gating and proton uptake by Wzx support O-antigen-subunit antiport
659 across the bacterial inner membrane. mBio **4:**e00678-00613.

660 40. **Islam ST, Lam JS.** 2013. Wzx flippase-mediated membrane translocation of sugar
661 polymer precursors in bacteria. Environ. Microbiol. **15:**1001-1015.

662 41. **Woodward R, Yi W, Li L, Zhao G, Eguchi H, Sridhar PR, Guo H, Song JK, Motari**
663 **E, Cai L, Kelleher P, Liu X, Han W, Zhang W, Ding Y, Li M, Wang PG.** 2010. *In vitro*
664 bacterial polysaccharide biosynthesis: defining the functions of Wzy and Wzz. Nat. Chem.
665 Biol. **6:**418-423.

666 42. **Islam ST, Gold AC, Taylor VL, Anderson EM, Ford RC, Lam JS.** 2011. Dual
667 conserved periplasmic loops possess essential charge characteristics that support a catch-
668 and-release mechanism of O-antigen polymerization by Wzy in *Pseudomonas aeruginosa*
669 PAO1. J. Biol. Chem. **286:**20600-20605.

670 43. **Islam ST, Huszczynski SM, Nugent T, Gold AC, Lam JS.** 2013. Conserved-residue
671 mutations in Wzy affect O-antigen polymerization and Wzz-mediated chain-length
672 regulation in *Pseudomonas aeruginosa* PAO1. Sci. Rep. **3:**3441.

673 44. **Cuthbertson L, Mainprize IL, Naismith JH, Whitfield C.** 2009. Pivotal roles of the
674 outer membrane polysaccharide export and polysaccharide copolymerase protein families
675 in export of extracellular polysaccharides in Gram-negative bacteria. Microbiol. Mol. Biol.
676 Rev. **73:**155-177.

677 45. **Kato T, Shirakawa Y, Takegawa K, Kimura Y.** 2015. Functional analysis of conserved
678 motifs in a bacterial tyrosine kinase, BtkB, from *Myxococcus xanthus*. J. Biochem.
679 **158:**385-392.

680 46. **Kimura Y, Kato T, Mori Y.** 2012. Function analysis of a bacterial tyrosine kinase, BtkB,
681 in *Myxococcus xanthus*. FEMS Microbiol. Lett. **336:**45-51.

682 47. **Kimura Y, Yamashita S, Mori Y, Kitajima Y, Takegawa K.** 2011. A *Myxococcus*
683 *xanthus* bacterial tyrosine kinase, BtkA, is required for the formation of mature spores. J.
684 Bacteriol. **193:**5853-5857.

685 48. **Standish AJ, Morona R.** 2014. The role of bacterial protein tyrosine phosphatases in the
686 regulation of the biosynthesis of secreted polysaccharides. Antioxid. Redox Signal.
687 **20:**2274-2289.

688 49. **Mori Y, Maeda M, Takegawa K, Kimura Y.** 2012. PhpA, a tyrosine phosphatase of
689 *Myxococcus xanthus*, is involved in the production of exopolysaccharide. Microbiology
690 **158:**2546-2555.

50. **Nickerson NN, Mainprize IL, Hampton L, Jones ML, Naismith JH, Whitfield C.** 2014. Trapped translocation intermediates establish the route for export of capsular polysaccharides across *Escherichia coli* outer membranes. Proc. Natl. Acad. Sci. USA **111:**8203-8208.

51. **Dong C, Beis K, Nesper J, Brunkan-LaMontagne AL, Clarke BR, Whitfield C, Naismith JH.** 2006. Wza the translocon for *E. coli* capsular polysaccharides defines a new class of membrane protein. Nature **444:**226.

52. **Yang Z, Geng Y, Xu D, Kaplan HB, Shi W.** 1998. A new set of chemotaxis homologues is essential for *Myxococcus xanthus* social motility. Mol. Microbiol. **30:**1123-1130.

53. **Yang Z, Li Z.** 2005. Demonstration of interactions among *Myxococcus xanthus* Dif chemotaxis-like proteins by the yeast two-hybrid system. Arch. Microbiol. **183:**243-252.

54. **Lancero HL, Castaneda S, Caberoy NB, Ma X, Garza AG, Shi W.** 2005. Analysing protein–protein interactions of the *Myxococcus xanthus* Dif signalling pathway using the yeast two-hybrid system. Microbiology **151:**1535-1541.

55. **Yang Z, Ma X, Tong L, Kaplan HB, Shimkets LJ, Shi W.** 2000. *Myxococcus xanthus dif* genes are required for biogenesis of cell surface fibrils essential for social gliding motility. J. Bacteriol. **182:**5793-5798.

56. **Bellenger K, Ma X, Shi W, Yang Z.** 2002. A CheW homologue is required for *Myxococcus xanthus* fruiting body development, social gliding motility, and fibril biogenesis. J. Bacteriol. **184:**5654-5660.

57. **Black WP, Wang L, Davis MY, Yang Z.** 2015. The orphan response regulator EpsW is a substrate of the DifE kinase and it regulates exopolysaccharide in *Myxococcus xanthus*. Sci. Rep. **5:**17831.

58. **Black WP, Yang Z.** 2004. *Myxococcus xanthus* chemotaxis homologs DifD and DifG negatively regulate fibril polysaccharide production. J. Bacteriol. **186:**1001-1008.

59. **Wu SS, Wu J, Kaiser D.** 1997. The *Myxococcus xanthus pilT* locus is required for social gliding motility although pili are still produced. Mol. Microbiol. **23:**109-121.

60. **Shimkets LJ.** 1986. Correlation of energy-dependent cell cohesion with social motility in *Myxococcus xanthus*. J. Bacteriol. **166:**837-841.

61. **Weimer RM, Creighton C, Stassinopoulos A, Youderian P, Hartzell PL.** 1998. A chaperone in the HSP70 family controls production of extracellular fibrils in *Myxococcus xanthus*. J. Bacteriol. **180:**5357-5368.

62. **Yang Z, Geng Y, Shi W.** 1998. A DnaK homolog in *Myxococcus xanthus* is involved in social motility and fruiting body formation. J. Bacteriol. **180:**218-224.

63. **Arnold JW, Shimkets LJ.** 1988. Cell surface properties correlated with cohesion in *Myxococcus xanthus*. J. Bacteriol. **170:**5771-5777.

64. **Overgaard M, Wegener-Feldbrügge S, Søgaard-Andersen L.** 2006. The orphan response regulator DigR is required for synthesis of extracellular matrix fibrils in *Myxococcus xanthus*. J. Bacteriol. **188:**4384-4394.

65. **Lu A, Cho K, Black WP, Duan X-y, Lux R, Yang Z, Kaplan HB, Zusman DR, Shi W.** 2005. Exopolysaccharide biosynthesis genes required for social motility in *Myxococcus xanthus*. Mol. Microbiol. **55:**206-220.

66. **Ward MJ, Lew H, Zusman DR.** 2000. Social motility in *Myxococcus xanthus* requires FrzS, a protein with an extensive coiled-coil domain. Mol. Microbiol. **37:**1357-1371.

67. **Rosenbluh A, Eisenbach M.** 1992. Effect of mechanical removal of pili on gliding motility of *Myxococcus xanthus*. J. Bacteriol. **174:**5406-5413.

68. **Shi W, Yang Z, Sun H, Lancero H, Tong L.** 2000. Phenotypic analyses of frz and dif double mutants of *Myxococcus xanthus*. FEMS Microbiol. Lett. **192:**211-215.

69. **Zhou T, Nan B.** 2017. Exopolysaccharides promote *Myxococcus xanthus* social motility by inhibiting cellular reversals. Mol. Microbiol. **103:**729-743.

70. **Black WP, Xu Q, Yang Z.** 2006. Type IV pili function upstream of the Dif chemotaxis pathway in *Myxococcus xanthus* EPS regulation. Mol. Microbiol. **61:**447-456.

71. **Rosenberg M, Gutnick D, Rosenberg E.** 1980. Adherence of bacteria to hydrocarbons: a simple method for measuring cell-surface hydrophobicity. FEMS Microbiol. Lett. **9:**29-33.

72. **Kupfer D, Zusman DR.** 1984. Changes in cell surface hydrophobicity of *Myxococcus xanthus* are correlated with sporulation-related events in the developmental program. J. Bacteriol. **159:**776-779.

73. **Kaczorek E, Pacholak A, Zdarta A, Smułek W.** 2018. The impact of biosurfactants on microbial cell properties leading to hydrocarbon bioavailability increase. Colloids Interfaces **2:**35.

74. **Behmlander RM, Dworkin M.** 1991. Extracellular fibrils and contact-mediated cell interactions in *Myxococcus xanthus*. J. Bacteriol. **173:**7810-7820.

75. **Kim S-H, Ramaswamy S, Downard J.** 1999. Regulated exopolysaccharide production in *Myxococcus xanthus*. J. Bacteriol. **181:**1496-1507.

76. **Dworkin M.** 1999. Fibrils as extracellular appendages of bacteria: their role in contact-mediated cell-cell interactions in *Myxococcus xanthus*. BioEssays **21:**590-595.

77. **Behmlander RM, Dworkin M.** 1994. Biochemical and structural analyses of the extracellular matrix fibrils of *Myxococcus xanthus*. J. Bacteriol. **176:**6295-6303.

78. **Dana JR, Shimkets LJ.** 1993. Regulation of cohesion-dependent cell interactions in *Myxococcus xanthus*. J. Bacteriol. **175:**3636-3647.

79. **Merroun ML, Ben Chekroun K, Arias JM, González-Muñoz MT.** 2003. Lanthanum fixation by *Myxococcus xanthus*: cellular location and extracellular polysaccharide observation. Chemosphere **52:**113-120.

80. **Mauriello EMF, Mignot T, Yang Z, Zusman DR.** 2010. Gliding motility revisited: how do the myxobacteria move without flagella? Microbiol. Mol. Biol. Rev. **74:**229-249.

81. **Gloag ES, Turnbull L, Javed MA, Wang H, Gee ML, Wade SA, Whitchurch CB.** 2016. Stigmergy co-ordinates multicellular collective behaviours during *Myxococcus xanthus* surface migration. Sci. Rep. **6:**26005.

82. **Gloag ES, Turnbull L, Whitchurch CB.** 2015. Bacterial stigmergy: an organising principle of multicellular collective behaviours of bacteria. Scientifica (Cairo) **2015:**387342.

83. **Kearns DB, Campbell BD, Shimkets LJ.** 2000. *Myxococcus xanthus* fibril appendages are essential for excitation by a phospholipid attractant. Proc. Natl. Acad. Sci. U. S. A. **97:**11505-11510.

84. **Fontes M, Kaiser D.** 1999. *Myxococcus* cells respond to elastic forces in their substrate. Proc. Natl. Acad. Sci. USA **96:**8052-8057.

85. **Lemon DJ, Yang X, Srivastava P, Luk Y-Y, Garza AG.** 2017. Polymertropism of rod-shaped bacteria: movement along aligned polysaccharide fibers. Sci. Rep. **7:**7643.

86. **Lemon DJ, Schutzman DA, Garza AG.** 2018. Bacterial surface spreading is more efficient on nematically aligned polysaccharide substrates. J. Bacteriol. **200:**e00610-00617.

87. **Luft JH.** 1971. Ruthenium red and violet. I. Chemistry, purification, methods of use for electron microscopy and mechanism of action. Anat. Rec. **171:**347-368.

88. **Burchard RP.** 1975. Myxospore induction in a nondispersed growing mutant of *Myxococcus xanthus*. J. Bacteriol. **122:**302-306.

89. **MacRae TH, McCurdy HD.** 1976. Evidence for motility-related fimbriae in the gliding microorganism *Myxococcus xanthus*. Can. J. Microbiol. **22:**1589-1593.

90. **Sun H, Zusman DR, Shi W.** 2000. Type IV pilus of *Myxococcus xanthus* is a motility apparatus controlled by the *frz* chemosensory system. Curr. Biol. **10:**1143-1146.

91. **Hu W, Hossain M, Lux R, Wang J, Yang Z, Li Y, Shi W.** 2011. Exopolysaccharide-independent social motility of *Myxococcus xanthus*. PLoS ONE **6:**e16102.

791 92. **Guzzo M, Agrebi R, Espinosa L, Baronian G, Molle V, Mauriello EMF, Brochier-**
792 **Armanet C, Mignot T.** 2015. Evolution and design governing signal precision and
793 amplification in a bacterial chemosensory pathway. PLoS Genet. **11:**e1005460.

794 93. **Tréguier J, Bugnicourt L, Gay G, Diallo M, Islam ST, Toro A, David L, Théodoly O,**
795 **Sudre G, Mignot T.** 2019. Chitosan films for microfluidic studies of single bacteria and
796 perspectives for antibiotic susceptibility testing. mBio **10:**e01375-01319.

797 94. **Mercier R, Mignot T.** 2016. Regulations governing the multicellular lifestyle of
798 *Myxococcus xanthus*. Curr. Opin. Microbiol. **34:**104-110.

799 95. **Fassel TA, Edmiston Jr. CE.** 1999. Ruthenium red and the bacterial glycocalyx. Biotech.
800 Histochem. **74:**194-212.

801 96. **Hanke DE, Northcote DH.** 1975. Molecular visualization of pectin and DNA by
802 ruthenium red. Biopolymers **14:**1-17.

803 97. **Charuk JHM, Pirraglia CA, Reithmeier RAF.** 1990. Interaction of ruthenium red with
804 Ca^{2+}-binding proteins. Anal. Biochem. **188:**123-131.

805 98. **Voelker D, Smejtek P.** 1996. Adsorption of ruthenium red to phospholipid membranes.
806 Biophys. J. **70:**818-830.

807 99. **Sutherland IW, Thomson S.** 1975. Comparison of polysaccharides produced by
808 *Myxococcus* strains. J. Gen. Microbiol. **89:**124-132.

809 100. **Gibiansky ML, Hu W, Dahmen KA, Shi W, Wong GCL.** 2013. Earthquake-like
810 dynamics in *Myxococcus xanthus* social motility. Proc. Natl. Acad. Sci. USA **110:**2330-
811 2335.

812 101. **Hu W, Li L, Sharma S, Wang J, McHardy I, Lux R, Yang Z, He X, Gimzewski JK, Li**
813 **Y, Shi W.** 2012. DNA builds and strengthens the extracellular matrix in *Myxococcus*
814 *xanthus* biofilms by interacting with exopolysaccharides. PLOS ONE **7:**e51905.

815 102. **MacLean L, Perry MB, Nossova L, Kaplan H, Vinogradov E.** 2007. The structure of
816 the carbohydrate backbone of the LPS from *Myxococcus xanthus* strain DK1622.
817 Carbohydr. Res. **342:**2474-2480.

818 103. **Curtis PD, Atwood J, Orlando R, Shimkets LJ.** 2007. Proteins associated with the
819 *Myxococcus xanthus* extracellular matrix. J. Bacteriol. **189:**7634-7642.

820 104. **Ducret A, Quardokus EM, Brun YV.** 2016. MicrobeJ, a tool for high throughput
821 bacterial cell detection and quantitative analysis. Nat. Microbiol. **1:**16077.
822
823

824 **FIGURE LEGENDS**

825 **Figure 1. (A)** Motility and developmental phenotypes for various mutants with altered levels of
826 secreted polysaccharides. Top panels (upper): gliding motility flares on CYE 1.5% agar after 30
827 h (scale bar: 50 µm). Top panels (lower): magnified view of white hatched box in corresponding
828 upper panel showing furrows in the agar substratum containing transiting cell groups (scale bar:
829 10 µm). Arrowheads (▷) indicate furrows in the agar left by previously-transited cells and/or
830 cell groups, revealed by extreme oblique illumination of agar surface. Middle panels: T4P-
831 dependent swarm spreading on CYE 0.5% agar after 72 h (scale bar: 2 mm). Bottom panels:
832 fruiting body formation on CF 1.5% agar after 75 h (scale bar: 1 mm). **(B)** Bar graphs of
833 diameters of swarms grown on CYE 0.5% agar for T4P-dependent motility at 72 h. For each
834 strain, the mean value of 3 biological replicates (+/− SEM) is plotted. Asterisks (*) denote
835 datasets displaying statistically significant differences ($p < 0.0001$) relative to both WT and
836 Δ*difG* strains, as determined via unpaired two-tailed Student's t-test analyses.
837
838 **Figure 2.** Auto-aggregation profiles of WT, EPS$^-$ (Δ*wzaX*), BPS$^-$ (Δ*wzaB*), and Ω*pilA* strains
839 resuspended in **(A)** CYE rich medium (mean values of 6, 6, 6, and 5 biological replicates [+/−
840 SEM], respectively) and **(B)** TPM minimal buffer (mean values of 3 biological replicates [+/−
841 SEM]). **(C)** Representative transmission electron micrographs of WT, BPS$^-$ (Δ*wzaB*), and EPS$^-$
842 (Δ*wzaX*) cells on copper grids, taken at 10 000× magnification (scale bar: 500 nm). Arrowheads
843 (▷) denote thin (likely single) T4P filaments. Arrows (⇨) denote thick (likely bundled) T4P
844 filaments. Asterisks (*) denote cell poles. **(D)** Boxplots of Trypan Blue dye retention to indicate
845 the levels of EPS production in various strains relative to WT. The lower and upper boundaries
846 of the boxes correspond to the 25th and 75th percentiles, respectively. The median (line through

centre of boxplot) and mean (+) of each dataset are indicated. Lower and upper whiskers represent the 10th and 90th percentiles, respectively; data points above and below the whiskers are drawn as individual points. Asterisks denote datasets displaying statistically significant differences in distributions ($p < 0.05$) shifted higher (**) or lower (*) than WT, as determined via Wilcoxon signed-rank test performed relative to "100". Data for Δ*difE* and Δ*difG* was heretofore unreported and acquired at the same time as the published values for other strains (32), reproduced with permission. **(E)** Microbial adhesion to hydrocarbons (MATH) test of WT and BPS^{-} (Δ*wzaB*) strain binding to hexadecane; values are the mean of 3 biological replicates (+/− SEM). Mix 1, initial pellet resuspension in CYE; Mix 2, supplemental control mixing; Mix 3, mixing upon addition of hexadecane ($t = 0$). Asterisk (*) denotes dataset displaying statistically significant difference in time point mean value ($p = 0.0176$) compared to WT, as determined via unpaired Student's t test. **(F)** Scanning electron micrographs of WT, EPS^{-} (Δ*wzaX*), and BPS^{-} (Δ*wzaB*) cells, taken at 20 000× magnification (scale bar: 1.0 µm). Arrows denote EPS fibrils connecting cells. Arrowheads denote potential surface-associated fibril material not engaged in inter-cell connections.

Figure 3. (A) Violin plots of single-cell gliding event speeds for WT, EPS^{-} (Δ*wzaX*), and BPS^{-} (Δ*wzaB*) cells on 1.5% agar pads (n = 2298 events across 4 biological replicates). A gliding event was defined as an instance of continuous translocation in a given direction. Cessation of motion by a given cell, followed by either a resumption of gliding in the same direction or a reversal of gliding direction, was considered the beginning of a new gliding event. The lower and upper boundaries of the plots correspond to the minimum and maximum values of the dataset, with the 25th and 75th percentiles displayed (*thick hatched black lines*). The median

(*solid black line*) and mean (+) of each dataset are indicated. Asterisks denote datasets displaying statistically significant differences in distributions ($p < 0.0001$) between (*) WT and EPS^-/BPS^- cells, as well as between (**) EPS^- and BPS^- cells, as determined via unpaired two-tailed Mann-Whitney test. **(B)** Boxplots of reversals per minute for tracked WT, EPS^-, and BPS^- single cells on 1.5% agar pads (n = 1135 cells across 4 biological replicates). The lower and upper boundaries of the boxes correspond to the 25th and 75th percentiles, respectively. The median (line through centre of boxplot) and mean (+) of each dataset are indicated. Lower and upper whiskers represent the 10th and 90th percentiles, respectively; data points above and below the whiskers are drawn as individual points. Asterisks denote datasets displaying statistically significant differences in distributions between (*) WT and EPS^- cells ($p = 0.0424$), (**) WT and BPS^- cells ($p < 0.0001$), and (***) EPS^- and BPS^- cells ($p < 0.0001$), as determined via unpaired two-tailed Mann-Whitney tests. **(C)** Violin plots of polymertropism responses for WT, EPS^- (Δ*wzaX*), and BPS^- (Δ*wzaB*) polysaccharide secretion mutant strains. The lower and upper boundaries of the plots correspond to the minimum and maximum values of the dataset, with the 25th and 75th percentiles displayed (*thick hatched black lines*). The median (*solid black line*) and mean (+) of each dataset are indicated. Asterisks denote datasets displaying statistically significant differences in distributions between (*) WT and BPS^- swarms ($p = 0.0006$) and (**) EPS^- and BPS^- swarms ($p = 0.0232$), whereas distributions between WT and EPS^- swarms were not significantly different ($p = 0.0845$), as determined via unpaired two-tailed Mann-Whitney test. The number of biological replicates (*n*) used to analyze each strain as follows: WT (11), Δ*wzaX* (10), Δ*wzaB* (10).

892 **Figure 4.** TEM analysis of Ruthenium Red-stained transverse sections cut from WT, MASC^{-}
893 (Δ*wzaS*), BPS^{-} (Δ*wzaB*), and EPS^{-} (Δ*wzaX*) swarms. Left-side panels, *inset*: relative position of
894 sample sectioning prior to TEM. Left-side panels: wide-angle views at 4000× magnification of
895 internal swarm architecture. For reference, the agar substratum and the apical face of the swarm
896 were located at the bottom and top (respectively) of each image. Scale bar: 1 µm. Right-side
897 panels: magnified views (20 000×) of the corresponding zone within white hatched boxes in the
898 left-side panels. Scale bar: 100 nm. Arrows (→) denote wispy putative polysaccharide-like
899 material. Filled arrowheads (▷) denote OMVs. Chevrons (>) denote OMV chains.

AUTHOR CONTRIBUTIONS

FS and STI conceived of and planned the study.

FS and NYJ performed stereoscopic phenotypic analyses and measured colony surface areas.

AN, FS, and NYJ prepared samples for electron microscopy

AN, FS, and NYJ performed transmission electron microscopy, while the former two performed scanning electron microscopy.

FS performed dye-binding assays.

STI performed auto-aggregation analyses.

FS tested strain hydrophobicity.

NYJ quantified cell motility and cell reversals.

DJL tested polymertropism responses, with analysis by STI and DJL.

FS, NYJ, and STI wrote the manuscript.

FS, NYJ, and STI generated figures.

STI, AGG, and FJV contributed personnel and funding support.

FIGURE 1

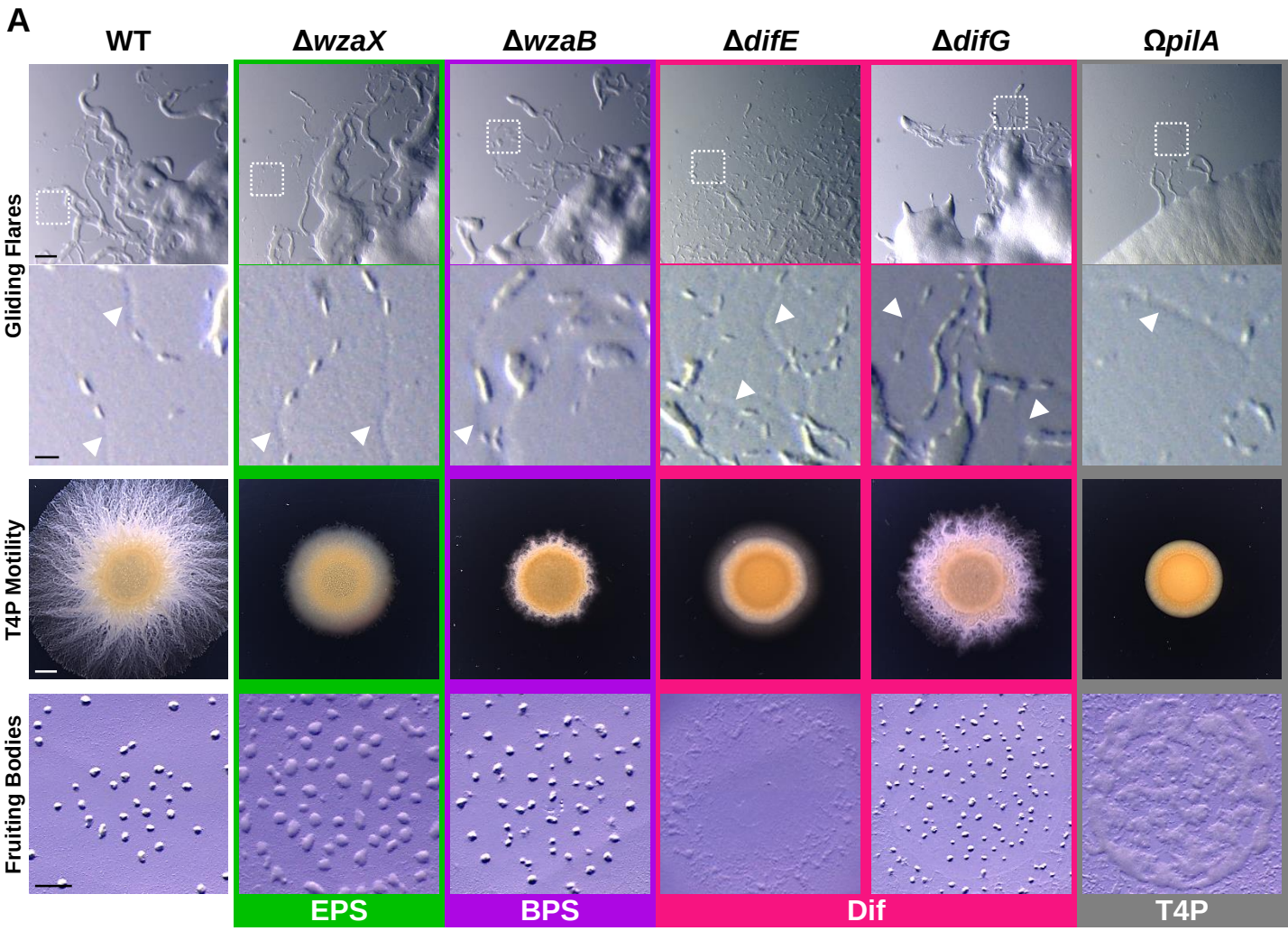
A
WT
ΔwzaX
ΔwzaB
ΔdifE
ΔdifG
ΩpilA
Gliding Flares
T4P Motility
Fruiting Bodies
EPS
BPS
Dif
T4P

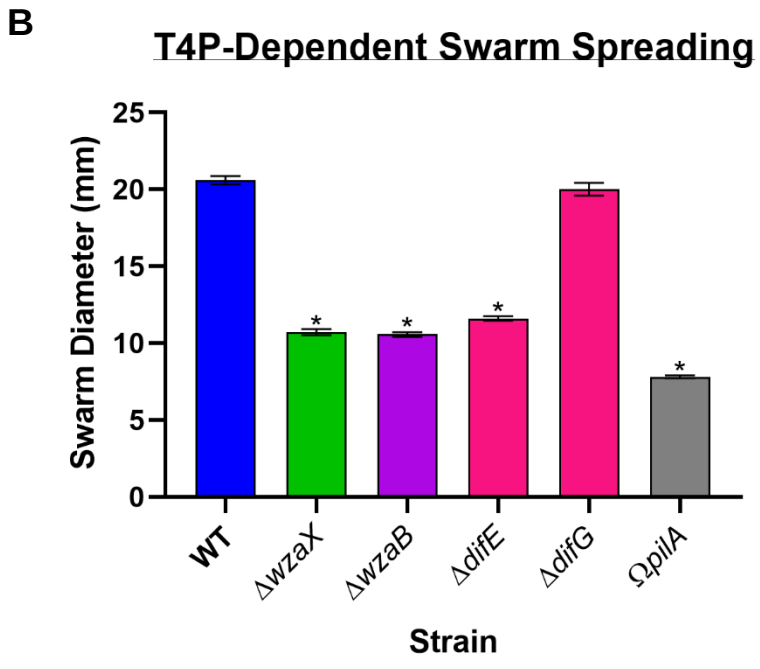
B
T4P-Dependent Swarm Spreading
Swarm Diameter (mm)
25
20
15
10
5
0
*
WT
ΔwzaX
ΔwzaB
ΔdifE
ΔdifG
ΩpilA
Strain

FIGURE 2

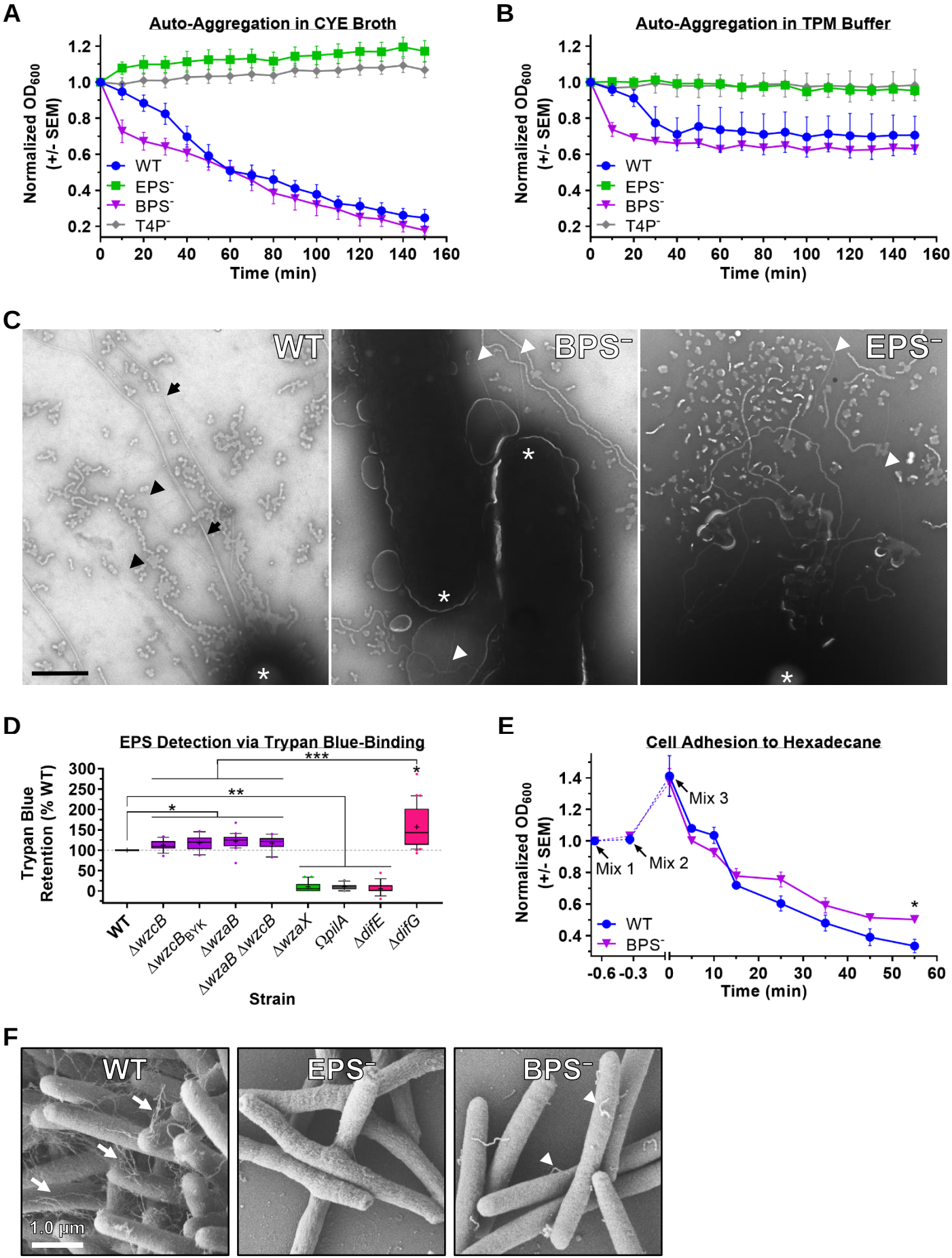
A
Auto-Aggregation in CYE Broth
Normalized OD600 (+/- SEM)
Time (min)
WT
EPS-
BPS-
T4P-
B
Auto-Aggregation in TPM Buffer
C
WT
BPS-
EPS-
D
EPS Detection via Trypan Blue-Binding
Trypan Blue Retention (% WT)
Strain
WT
ΔwzcB
ΔwzcBBYK
ΔwzaB
ΔwzaB ΔwzcB
ΔwzaX
ΩpilA
ΔdifE
ΔdifG
E
Cell Adhesion to Hexadecane
Mix 1
Mix 2
Mix 3
F
1.0 µm

FIGURE 3

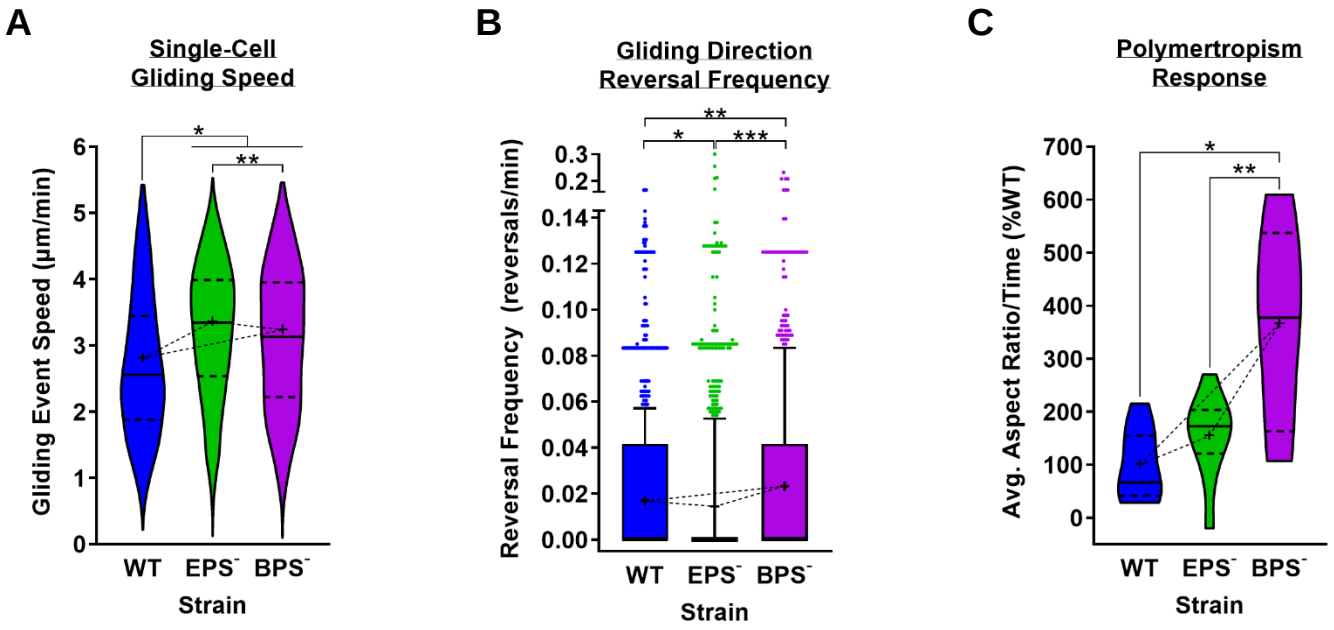
A
Single-Cell
Gliding Speed
Gliding Event Speed (µm/min)
0
1
2
3
4
5
6
*
**
WT
EPS-
BPS-
Strain
B
Gliding Direction
Reversal Frequency
Reversal Frequency (reversals/min)
0.00
0.02
0.04
0.06
0.08
0.10
0.12
0.14
0.2
0.3
**
*
***
WT
EPS-
BPS-
Strain
C
Polymertropism
Response
Avg. Aspect Ratio/Time (%WT)
0
100
200
300
400
500
600
700
*
**
WT
EPS-
BPS-
Strain

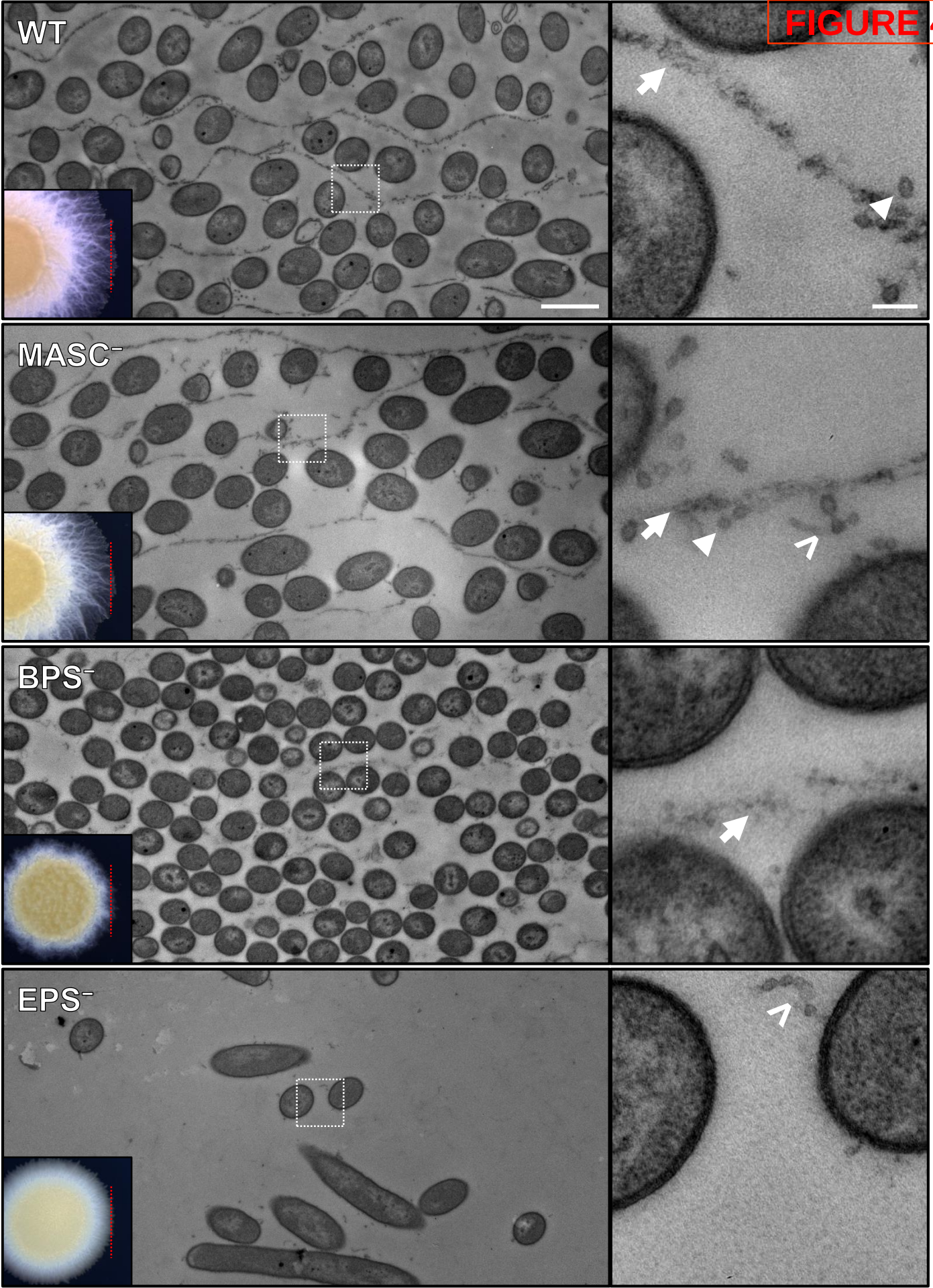
FIGURE 4
WT
MASC⁻
BPS⁻
EPS⁻

TABLE 1

Strain Code	Strain	Genotype/ Description	Source or Reference
TM108	*Myxococcus xanthus* DZ2	Wild type	Laboratory collection
TM469	Δ*wzaX*	Δ*mxan_7417/epsY*	[1]
TM484	Δ*wzaS*	Δ*mxan_3225/exoA/fdgA*	[1]
TM529	Δ*wzaB*	Δ*mxan_1915*	[1]
EM450	Δ*difE*	Δ*mxan_6692*	[2]
EM451	Δ*difG*	Δ*mxan_6691*	Laboratory collection
TM293	Ω*pilA*	Ω*mxan_5783* (Tet^R cassette insertion)	Laboratory collection

[1] Ducret A, Valignat M-P, Mouhamar F, Mignot T, Theodoly O. Wet-surface-enhanced ellipsometric contrast microscopy identifies slime as a major adhesion factor during bacterial surface motility. Proc. Natl. Acad. Sci. U. S. A. 2012. 109(25):10036-10041.

[2] Moine A, Agrebi R, Espinosa L, Kirby JR, Zusman DR, Mignot T, Mauriello EMF. Functional organization of a multimodular bacterial chemosensory apparatus. PLOS Genet. 2014. 10(3):e1004164